

Correlated Topological States in Graphene Nanoribbon Heterostructures

Jan-Philip Joost,[†] Antti-Pekka Jauho,[‡] and Michael Bonitz^{*,†}

[†]*Institut für Theoretische Physik und Astrophysik, Christian-Albrechts-Universität zu Kiel, D-24098 Kiel, Germany*

[‡]*CNG, DTU Physics, Technical University of Denmark, Kongens Lyngby, DK 2800, Denmark*

E-mail: bonitz@theo-physik.uni-kiel.de

Abstract

Finite graphene nanoribbon (GNR) heterostructures host intriguing topological in-gap states (Rizzo, D. J. et al. *Nature* **2018**, 560, 204]). These states may be localized either at the bulk edges, or at the ends of the structure. Here we show that correlation effects (not included in previous density functional simulations) play a key role in these systems: they result in increased magnetic moments at the ribbon edges accompanied by a significant energy renormalization of the topological end states – even in the presence of a metallic substrate. Our computed results are in excellent agreement with the experiments. Furthermore, we discover a striking, novel mechanism that causes an energy splitting of the non-zero-energy topological end states for a weakly screened system. We predict that similar effects should be observable in other GNR heterostructures as well.

Introduction. Strongly correlated materials host exciting physics such as superconductivity or the fractional quantum Hall effect.¹ While in monolayer graphene electron correlations are weak,² carbon based finite systems and heterostructures can exhibit flat bands near the Fermi energy resulting in nontrivial correlated phases.^{3,4} One example are magic-angle twisted graphene bilayers where localized electrons lead to Mott-like insulator states and un-

conventional superconductivity.^{5–7} Another exciting class of systems that has been predicted to host strongly localized phases are graphene nanoribbon (GNR) heterostructures.^{8–14} Similar to topological insulators they combine an insulating bulk with robust in-gap boundary states^{15,16} and are expected to host Majorana fermions in close proximity to a superconductor.¹⁷ Recently, it was confirmed that GNR heterostructures composed of alternating segments of 7- and 9-armchair GNRs (AGNRs), as sketched in Fig. 1(a), exhibit new topological bulk bands and end states that differ qualitatively from the band structures of pristine 7- and 9-AGNRs.¹⁸

Although electronic correlations are expected to play a crucial role for the localized topological states in GNR heterostructures,¹⁹ so far, most theoretical work has been restricted to tight-binding (TB) models or density functional theory within the local density approximation (LDA-DFT) which are known to completely ignore or underestimate these effects. Here, we present a systematic analysis of electronic correlations in 7-9-AGNRs, based on a Green functions method with *GW* self-energy^{20,21} applied to an effective Hubbard model. We compute the differential conductance and find excellent agreement with the experimental measurements of Ref. 18. Our calculations reveal that, even in the presence of a screening Au(111) surface, local electronic correlations induce a strong en-

ergy renormalization of the band structure. Especially the topological end states localized at the heterostructure-vacuum boundary experience strong quasiparticle corrections which are not captured by LDA-DFT. For freestanding systems, or systems on an insulating surface, we predict that these states exhibit an energy splitting due to a magnetic instability at the Fermi energy. The local build-up of electronic correlations is further analyzed by considering the local magnetic moment at the ribbon edges. We also examine finite size effects and the origin of the topological end states by varying the system size and end configuration, respectively. On this basis we predict that a whole class of systems exists that can host end states with similar exciting properties.

Model. We consider the 7-9-AGNR heterostructure consisting of alternating 7-AGNR and 9-AGNR segments as depicted in Fig. 1(a). The system was realized experimentally on a metallic Au(111) surface by Rizzo *et al.*¹⁸ who observed topological in-gap states at the heterojunction between 7- and 9-AGNR segments (bulk), and at the termini of the heterostructure (end). While previous LDA-DFT simulations describe reasonably well the bulk bands, they do not reproduce quantitatively the experimental energies of the end states (see below). To overcome these limitations, we apply a recently developed Green functions approach which gives access to spectral and magnetic properties of the system, see, e.g. Refs. 20,22,23. The electronic system is described with an effective Hubbard model, the Hamiltonian of which is expressed in terms of the operators $\hat{c}_{i\alpha}^\dagger$ and $\hat{c}_{j\alpha}$ that create and annihilate an electron with spin projection α at site i and j , respectively,

$$\hat{H} = -J \sum_{\langle i,j \rangle, \alpha} \hat{c}_{i\alpha}^\dagger \hat{c}_{j\alpha} + U \sum_i \hat{c}_{i\uparrow}^\dagger \hat{c}_{i\uparrow} \hat{c}_{i\downarrow}^\dagger \hat{c}_{i\downarrow}, \quad (1)$$

where $J = 2.7$ eV is the hopping amplitude between adjacent lattice sites,²⁴ and U is the on-site interaction. The edges of the GNR are assumed to be H-passivated. Observables can be computed from the Green function $\mathbf{G}(\omega)$ that is defined in terms of the operators $\hat{c}_{i\alpha}^\dagger$ and

$\hat{c}_{j\alpha}$, for details see the Supporting Information (SI). Correlation effects are included via the self-energy Σ which enters in the self-consistent Dyson equation^{22,23}

$$\mathbf{G}(\omega) = \mathbf{G}_0(\omega) + \mathbf{G}_0(\omega)\Sigma(\omega)\mathbf{G}(\omega), \quad (2)$$

where the single-particle Green function \mathbf{G} contains the spectral and magnetic information of the system, and \mathbf{G}_0 is its non-interacting limit. In the present work we report the first full GW-simulations of the system (1, 2) for experimentally realized GNR heterostructures, as the one shown in Fig. 1(a). The details of the numerical procedure are provided in the SI.

In what follows, we compare the tight-binding (TB), unrestricted Hartree-Fock (UHF), and *GW* approximations for Σ , in order to quantify electronic correlation effects. The TB approach, corresponding to setting $U = 0$, is often used to describe GNRs, due to its simplicity,^{17,25–27} and here serves as a point of reference for the uncorrelated system. For *GW* the on-site interaction was chosen such that it reproduces the experimental bulk band gap of Ref. 18, resulting in $U = 2.5J$, see SI. This choice of U also takes into account screening effects of the metallic substrate. The description of free-standing GNRs within *GW* requires a larger on-site interaction²⁸ which makes the selfconsistent solution of Eq. (2) more challenging. Nonetheless, to get a qualitative understanding of the properties of free-standing heterojunctions we employ the UHF approximation which is known to qualitatively describe edge magnetism in free-standing ZGNRs. For this case the on-site interaction was chosen as $U = 1J$.²⁹ The spatially resolved dI/dV data, recorded in an STM experiment, are generated by placing $2p_z$ orbitals on top of the atomic sites of the lattice structure, following the procedures described in Refs. 30,31.

Quasiparticle renormalization. In Figs. 1(b) and (c) we present differential conductance results for the 7-9-AGNR heterostructure on Au(111), comparing TB, UHF and *GW* simulations to the experiment of Ref. 18.¹ Our

¹In the experiment the ribbon was slightly doped

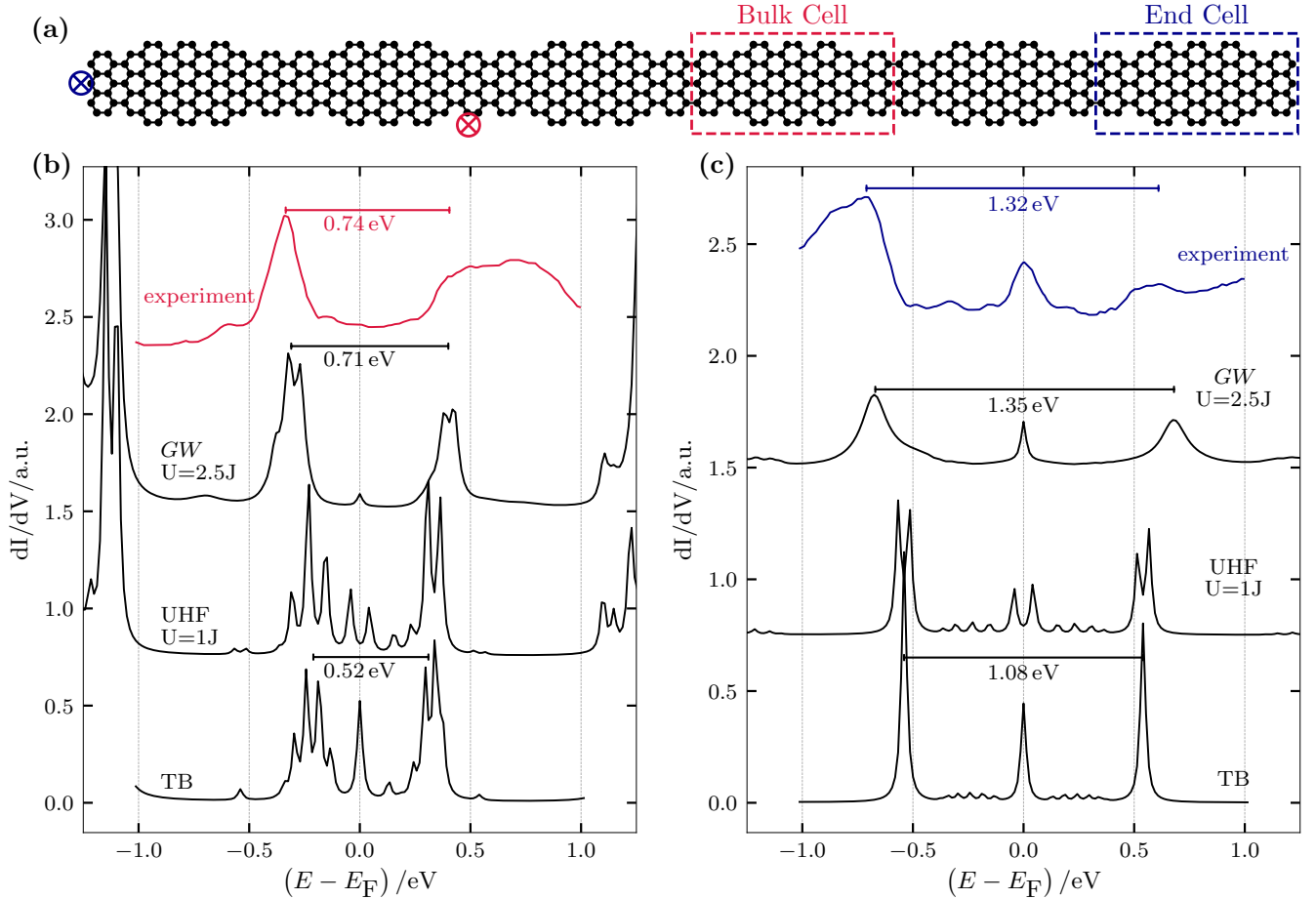


Figure 1: (a) 7-9-AGNR heterostructure containing six unit cells. The red [blue] cross marks the position of the dI/dV spectra shown in (b) [(c)]. The red (blue) dashed rectangle marks the bulk (end) unit cell referenced in Fig. 3. (b) dI/dV spectrum measured (red) and simulated (black) at the position in the bulk region marked by the red cross in (a). (c) dI/dV spectrum measured (blue) and simulated (black) at the position in the end region marked by the blue cross in (a). The curves in (b) and (c) are shifted vertically, for better comparison. The experimental data are taken from Ref. 18 and corrected for charge doping effects.

calculations were performed for a system containing six unit cells as shown in Fig. 1(a). In accordance with the measurements the results for the bulk (end) calculation are averaged over the area marked by the red (blue) cross. In the experiment, a band gap of $E_{g,\text{bulk}}^{\text{exp}} = 0.74 \text{ eV}$ between the bulk bands is observed whereas the gap between the non-zero energy end peaks is $E_{g,\text{end}}^{\text{exp}} = 1.32 \text{ eV}$. The TB approximation vastly underestimates the gaps, with $E_{g,\text{bulk}}^{\text{TB}} = 0.52 \text{ eV}$ and $E_{g,\text{end}}^{\text{TB}} = 1.08 \text{ eV}$, respectively. In addition

which shifts the dI/dV spectrum to higher energies. Our calculations were performed for half filling. For comparison the experimental data was shifted so that the zero-energy peaks of theory and experiment match.

to the two bands in the bulk region an additional unphysical zero-energy mode appears in the TB solution.

Next, we include mean-field effects within the UHF approximation. This does not lead to a considerable energy renormalization for the bulk and end states, but to a splitting of all three topological states which are localized at the end of the heterostructure, cf. Fig. 1(c). The behaviour of the two non-zero energy end peaks is particularly surprising. While the splitting of the zero-energy edge peaks in ZGNRs is well known³² and is attributed to magnetic instabilities at the Fermi level,³³ the splitting of states at non-zero energy cannot be understood

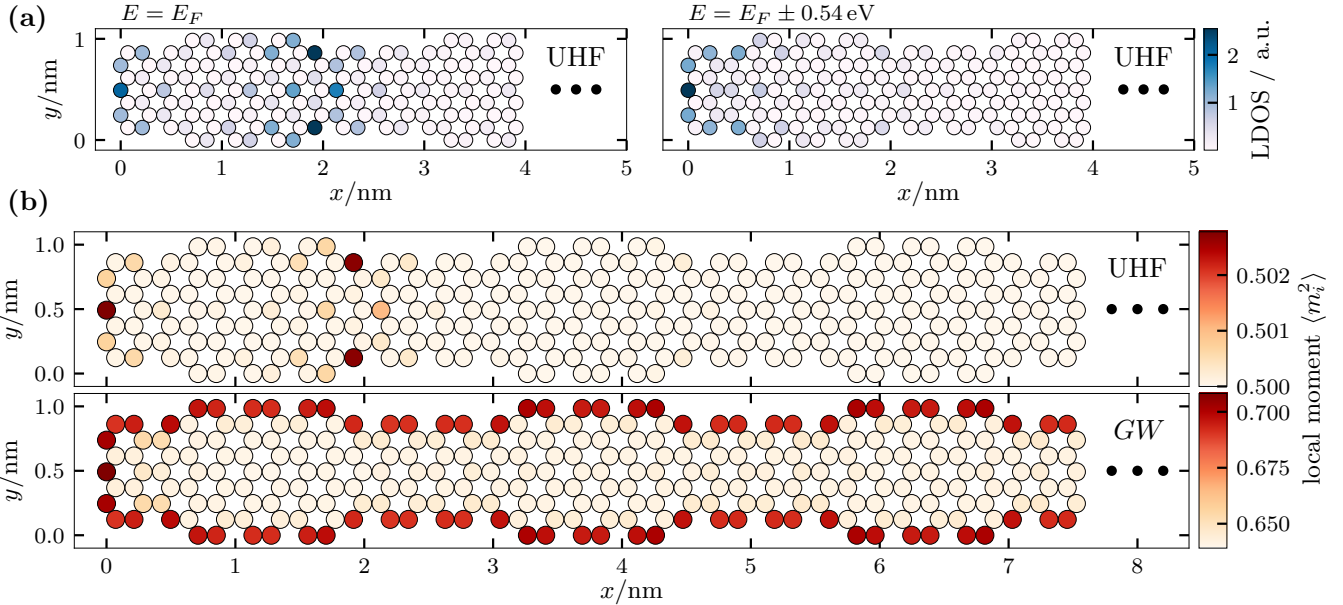


Figure 2: (a) LDOS of the topological end states at $E = E_F$ (left) and $E = E_F \pm 0.54$ eV (right) for UHF as shown in Fig. 1(c). (b) Local moment $\langle m_i^2 \rangle$, Eq. (3), of the 7-9-AGNR of Fig. 1(a) calculated within UHF (top) and *GW* (bottom). Since the ribbon is symmetric only three of the six unit cells are shown as indicated by the three black dots.

in this picture. In the experimental data where the system is on top of a screening Au(111) surface this effect is not observed. However, metallic substrates are known to suppress the splitting of zero-energy states in finite length pristine AGNRs³⁴ compared to insulating substrates.³⁵ The UHF result indicates that a splitting of all three end peaks, as seen in Fig. 1(c), will emerge in measurements for an insulated heterojunction.

Finally, including quasiparticle corrections within the *GW* approximation results in a considerable correlation-induced renormalization of both the bulk and end states. The observed gaps of $E_{\text{g,bulk}}^{\text{GW}} = 0.71$ eV and $E_{\text{g,end}}^{\text{GW}} = 1.35$ eV are in excellent agreement with the experimental findings. Additionally, *GW* correctly reduces the unphysical zero-energy contribution in the bulk and prevents the splitting of the end states through selfconsistent screening².

Local correlations. To understand the

²One should note that the extreme broadening of the upper bulk band seen in the experiment is not captured by our simulations. The origin of this broadening is unclear at present, however it is probably caused by the experimental setup, i.e. the substrate or the tip.

mechanisms causing the above mentioned renormalization and splitting of the topological states, we next consider local correlations and magnetic polarizations. In Fig. 2(b) we compare the local moment at site i

$$\langle \hat{m}_i^2 \rangle = \langle (\hat{n}_{\uparrow,i} - \hat{n}_{\downarrow,i})^2 \rangle = \rho_i - 2D_i, \quad (3)$$

from UHF- and *GW*-simulations for the same system as in Fig. 1. The local moment quantifies the local interaction energy and is a measure of the local magnetic polarization of the system. It is directly related to the local density ρ_i and double occupation D_i at site i [cf. Eq. (3)] which are strongly affected by electronic correlations. Consequently, the local moment is, in general, higher for *GW* than for UHF. In the latter case the local moment is peaked exactly at the sites where the zero-energy end state is localized, which can be confirmed by comparing to the LDOS in Fig. 2(a). Considering the splitting of the zero-energy end peak in Fig. 1(c) this is in agreement with previous mean-field calculations for ZGNRs^{33,36} where the magnetic instability of the zero-energy edge state gives rise to an antiferromagnetic ordering at opposing zigzag edges. However, such an instability

does not occur for the non-zero end states for which the local distribution only partially coincides with the local moment, cf. Fig 2(a). Instead, the splitting of these states observed in Fig. 1(c) originates from their hybridization with the zero-energy zigzag state which is further investigated in the discussion of Fig. 4. Strikingly, for *GW* the local moment is increased on all edges of the heterostructure, which coincides with the regions where the topological states are localized, cf. Fig. 4(b). Consequently, the renormalization of the topological bulk and end peaks can be attributed to strongly localized correlations at the edges of the heterostructure. The topological states that extend across the boundary of the heterostructure result in increased magnetic polarization even at the armchair edges of the ribbon. This surprising finding is in contrast to the prediction of the UHF simulation in this work and other mean-field theory results^{29,33,37–40} where typically considerable magnetic polarization is only observed at the zigzag edges of GNRs.

Finite size effects. The GNR heterostructure discussed in Figs. 1 and 2 contains six unit cells, exactly as in the experiments. In the following we explore the effect of the system size on the topological states. In Fig. 3 the local density of states (LDOS) of heterostructures containing one to eight unit cells is shown for the bulk and end cells comparing TB and *GW* results. For the eight unit cell system, additionally, the LDA-DFT result of Ref. 18 is plotted to allow for a direct comparison to our results. The observed effects differ for the two regions of the system. The spectral weight of the bulk bands increases with system size. In fact, the TB results, that show the total DOS, indicate that the number of peaks in the bulk bands corresponds to the number of bulk unit cells. This is in agreement with the idea that the bulk bands form by hybridization of heterojunction states of adjacent bulk cells. For *GW* the energies of the bulk states are renormalized and broadened by electronic correlations, as shown in Fig. 1.

In the end cell the three topological states are stable for systems of three or more unit

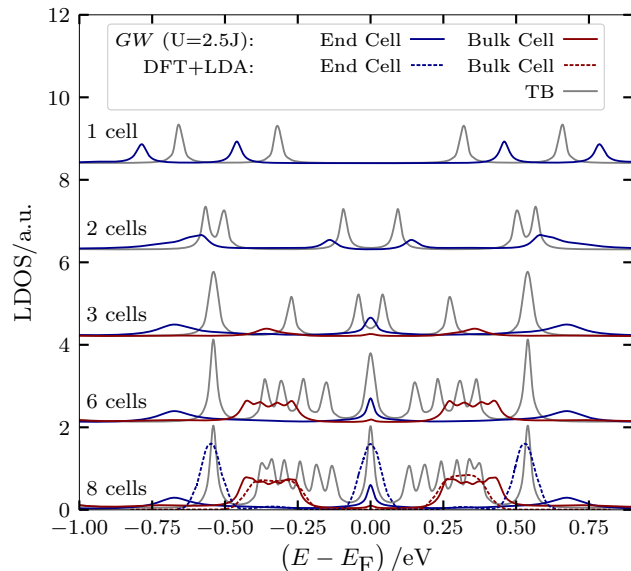


Figure 3: LDOS for 7-9-AGNR heterostructures consisting of one to eight unit cells. The case of six unit cells is the one shown in Fig. 1(a). Red (blue) lines: bulk (end) cell results as shown in Fig. 1(a). Solid (dashed): *GW* (LDA-DFT) calculations. The DFT results are taken from Ref. 18. Solid grey lines: total DOS from TB calculations. The lines for different systems are shifted vertically for better comparison.

cells. For these large systems the states on both ends of the ribbon are separated by bulk cells. However, for smaller systems the states of opposing termini overlap and result in an additional splitting of the end states. In addition to this topological effect, the energies of the end states are also renormalized due to electronic correlations, in general resulting in higher energies of the states. However, interestingly, for the intermediate system of three unit cells the splitting of the zero-energy state is reduced for the correlated *GW*-result as compared to TB. This is the result of a competition of both aforementioned effects. Within *GW* the spatial extension of the zero-energy state is strongly reduced, cf. Fig 1(b) and SI, resulting in a significantly smaller overlap and finite-size splitting of the states on both ends of the system.

Comparing the results of *GW* and LDA-DFT

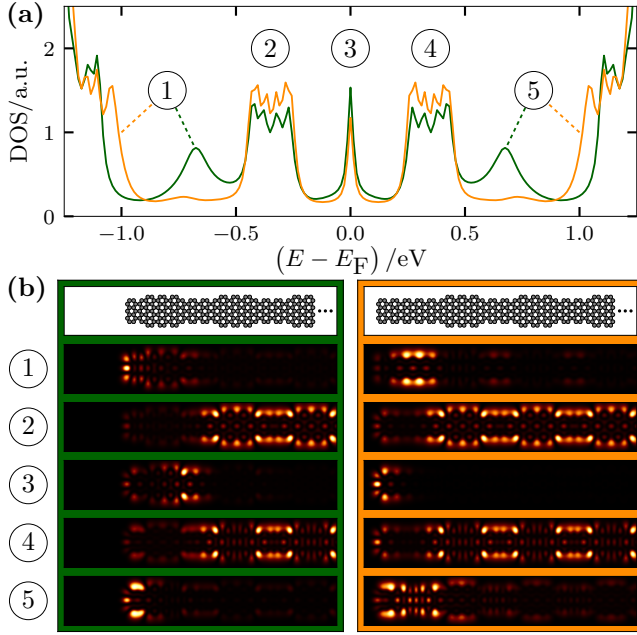


Figure 4: (a) Total DOS calculated with *GW* and $U = 2.5J$ for the two systems indicated in the top panel of (b). The green (orange) line corresponds to the left (right) system. The left system contains exactly six unit cells while the right system is extended additionally by ten zigzag lines on both sides. (b) dI/dV maps for the same two systems. The maps labelled 1-5 correspond to the labelled peaks in (a). Only a small section of the ribbon is shown indicated by the three black dots in the top panel.

for the eight unit cell system reveals that LDA-DFT captures reasonably well the renormalization of the bulk band energies whereas it completely fails to describe the shift of the end states. This indicates that a correct characterization of these topological end states is particularly challenging and requires an accurate description of the underlying electronic correlations.

Topological end states. Since the topological states at the end of the heterostructure are found to be particularly sensitive to electron-electron interactions it is important to examine in detail the origin of these states. The emergence of topological end states at the termini of GNR heterostructures can be explained by the \mathbb{Z}_2 invariant and the bulk-boundary correspondence of topological insulator theory.¹⁰ However, to get a better understanding of their

properties, in the following, the specific mechanism that leads to the existence of these multiple end states will be analyzed. For this, in Fig. 4 the total DOS (a) and the dI/dV maps (b) of the heterostructure containing six unit cells (green) are compared to the same system with an additional ten zigzag lines on each side of the ribbon (orange) for *GW*. The two systems are depicted in the topmost panel of Fig. 4(b). Comparing the DOS it stands out that the high-energy end peaks, that are present in the six unit cell system, are strongly suppressed in the longer system. Instead a new high-energy peak emerges around ± 1 eV. Additionally, the spectral weight of the bulk bands is increased for the longer system. All these observations can be understood from the dI/dV maps of the states in Fig. 4(b). For the longer system the zigzag edge at the end of the system is separated from the heterojunction of the first unit cell by a long 7-AGNR section. Due to this clear separation the three end states (1, 3, 5) resemble states observed in pristine 7-AGNR, see SI. Furthermore, the heterojunction states of all six unit cells hybridize to form the bulk bands (2, 4). In contrast, for the shorter system the adjacent states localized at the zigzag edge and at the heterojunctions of the first unit cell can overlap leading to three hybridized states in the termini of the system. As a consequence the bulk bands are localized only in the four inner bulk unit cells and do not occupy the end cells resulting in a reduced spectral weight in the DOS.

Splitting of peaks induced by the spatial overlap of the associated states typically appears in small finite systems, cf. Fig. 3 for one unit cell. Strikingly, due to the close proximity of finite substructures, i.e. heterojunctions and ribbon edges, the same effect emerges at the termini of large heterostructures containing hundreds to thousands of atoms. Consequently, this observation is not restricted to the present 7-9-AGNR heterostructures. Instead, we predict that similar strongly correlated states exist also in an entire class of systems which meet the criteria for hosting hybridized end states, i.e. possess topological states close to localized edge

states. The existence of such states is determined by the topology of the system.^{10,41,42}

Summary and discussion. We analyzed the influence of electronic correlations on the topological states of 7-9-AGNR heterostructures on Au(111). While the general topological structure of the system, previously predicted on the TB level,¹⁰ remains stable, additional new effects connected to the topological states emerge. Our *GW* simulations reveal that strong local electronic correlations are present in both the edges of the bulk and the end region of the heterostructure resulting in increased magnetic moments in the zigzag and armchair edges. Strikingly, the spatially confined topological states of the termini are more severely affected by these correlations than the extended topological bulk bands. For the latter we found, by comparison to our *GW* results, that LDA-DFT is able to reproduce the experimental dI/dV measurements since quasiparticle corrections are weak, in this case. In contrast, the topological end states, emerging due to the hybridization of zigzag-edge and heterojunction states, are strongly renormalized and screened due to electronic correlations which gives rise to a large discrepancy between LDA-DFT and experimental energies. For free-standing heterostructures we find a new mechanism that leads to the splitting of non-zero energy states due to hybridization with a zero-energy state. These findings are not restricted to the specific system considered here but instead are expected to be present in similar GNR heterostructures that exhibit strongly localized topological states.

Acknowledgement We acknowledge helpful discussions with Niclas Schlünzen. APJ is supported by the Danish National Research Foundation, Project DNRF103.

Supporting Information Available

The following files are available free of charge.

The following files are available free of charge.

- suppinfo.pdf: Details on the Green func-

tion approach, the fitting of the Hubbard interaction U , damping of the zero-energy state, and a comparison to 7-AGNR states.

References

- (1) Stormer, H. L.; Tsui, D. C.; Gossard, A. C. The fractional quantum Hall effect. *Rev. Mod. Phys.* **1999**, *71*, 298–305.
- (2) Das Sarma, S.; Adam, S.; Hwang, E. H.; Rossi, E. Electronic transport in two-dimensional graphene. *Rev. Mod. Phys.* **2011**, *83*, 407–470.
- (3) Neilson, D.; Perali, A.; Zarenia, M. Many-body electron correlations in graphene. *J. Phys.: Conf. Ser.* **2016**, *702*, 012008.
- (4) Balzer, K.; Rasmussen, M. R.; Schlünzen, N.; Joost, J.-P.; Bonitz, M. Doublon Formation by Ions Impacting a Strongly Correlated Finite Lattice System. *Phys. Rev. Lett.* **2018**, *121*, 267602.
- (5) Cao, Y.; Fatemi, V.; Demir, A.; Fang, S.; Tomarken, S. L.; Luo, J. Y.; Sanchez-Yamagishi, J. D.; Watanabe, K.; Taniguchi, T.; Kaxiras, E.; Ashoori, R. C.; Jarillo-Herrero, P. Correlated insulator behaviour at half-filling in magic-angle graphene superlattices. *Nature* **2018**, *556*, 80–84.
- (6) Cao, Y.; Fatemi, V.; Fang, S.; Watanabe, K.; Taniguchi, T.; Kaxiras, E.; Jarillo-Herrero, P. Unconventional superconductivity in magic-angle graphene superlattices. *Nature* **2018**, *556*, 43–50.
- (7) Kerelsky, A.; McGilly, L. J.; Kennes, D. M.; Xian, L.; Yankowitz, M.; Chen, S.; Watanabe, K.; Taniguchi, T.; Hone, J.; Dean, C.; Rubio, A.; Pasupathy, A. N. Maximized electron interactions at the magic angle in twisted bilayer graphene. *Nature* **2019**, *572*, 95–100.

- (8) Cai, J.; Pignedoli, C. A.; Talirz, L.; Ruffieux, P.; Söde, H.; Liang, L.; Meunier, V.; Berger, R.; Li, R.; Feng, X.; Müllen, K.; Fasel, R. Graphene nanoribbon heterojunctions. *Nature Nanotechnology* **2014**, *9*, 896–900.
- (9) Chen, Y.-C.; Cao, T.; Chen, C.; Pedramrazi, Z.; Haberer, D.; de Oteyza, D. G.; Fischer, F. R.; Louie, S. G.; Crommie, M. F. Molecular bandgap engineering of bottom-up synthesized graphene nanoribbon heterojunctions. *Nature Nanotechnology* **2015**, *10*, 156–160.
- (10) Cao, T.; Zhao, F.; Louie, S. G. Topological Phases in Graphene Nanoribbons: Junction States, Spin Centers, and Quantum Spin Chains. *Phys. Rev. Lett.* **2017**, *119*, 076401.
- (11) Jacobse, P. H.; Kimouche, A.; Gebraad, T.; Ervasti, M. M.; Thijssen, J. M.; Liljeroth, P.; Swart, I. Electronic components embedded in a single graphene nanoribbon. *Nature Communications* **2017**, *8*, 119.
- (12) Ma, C.; Liang, L.; Xiao, Z.; Poretzky, A. A.; Hong, K.; Lu, W.; Meunier, V.; Bernholc, J.; Li, A.-P. Seamless Staircase Electrical Contact to Semiconducting Graphene Nanoribbons. *Nano Lett.* **2017**, *17*, 6241–6247.
- (13) Wang, S.; Kharche, N.; Costa Girão, E.; Feng, X.; Müllen, K.; Meunier, V.; Fasel, R.; Ruffieux, P. Quantum Dots in Graphene Nanoribbons. *Nano Lett.* **2017**, *17*, 4277–4283.
- (14) Rizzo, D. J. et al. Length-Dependent Evolution of Type II Heterojunctions in Bottom-Up-Synthesized Graphene Nanoribbons. *Nano Lett.* **2019**, *19*, 3221–3228.
- (15) Hasan, M. Z.; Kane, C. L. Colloquium: Topological insulators. *Rev. Mod. Phys.* **2010**, *82*, 3045–3067.
- (16) Asbóth, J. K.; Oroszlány, L.; Pályi, A. *A Short Course on Topological Insulators: Band Structure and Edge States in One and Two Dimensions*; Lecture Notes in Physics; Springer: Cham, 2016; Vol. 919.
- (17) Gröning, O.; Wang, S.; Yao, X.; Pignedoli, C. A.; Borin Barin, G.; Daniels, C.; Cupo, A.; Meunier, V.; Feng, X.; Narita, A.; Müllen, K.; Ruffieux, P.; Fasel, R. Engineering of robust topological quantum phases in graphene nanoribbons. *Nature* **2018**, *560*, 209–213.
- (18) Rizzo, D. J.; Veber, G.; Cao, T.; Bronner, C.; Chen, T.; Zhao, F.; Rodriguez, H.; Louie, S. G.; Crommie, M. F.; Fischer, F. R. Topological band engineering of graphene nanoribbons. *Nature* **2018**, *560*, 204.
- (19) Lado, J. L.; Ortiz, R.; Fernández-Rossier, J. Emergent quantum matter in graphene nanoribbons. *arXiv:1909.00258 [cond-mat]* **2019**,
- (20) Stefanucci, G.; Leeuwen, R. v. *Nonequilibrium many-body theory of quantum systems: a modern introduction*; Cambridge University Press: Cambridge, 2013.
- (21) Schlünzen, N.; Hermanns, S.; Scharnke, M.; Bonitz, M. Ultrafast dynamics of strongly correlated fermions – Nonequilibrium green functions and selfenergy approximations. *J. Phys.: Cond. Matt.* **2019**,
- (22) Haug, H.; Jauho, A.-P. *Quantum Kinetics in Transport and Optics of Semiconductors*; Springer: Berlin, Heidelberg, 2008.
- (23) Balzer, K.; Bonitz, M. *Nonequilibrium Green's Functions Approach to Inhomogeneous Systems*; Springer: Berlin, Heidelberg, 2013.
- (24) Reich, S.; Maultzsch, J.; Thomsen, C.; Ordejón, P. Tight-binding description of graphene. *Phys. Rev. B* **2002**, *66*, 035412.

- (25) Xu, Z.; Zheng, Q.-S.; Chen, G. Elementary building blocks of graphene-nanoribbon-based electronic devices. *Appl. Phys. Lett.* **2007**, *90*, 223115.
- (26) Sevinçli, H.; Topsakal, M.; Ciraci, S. Superlattice structures of graphene-based armchair nanoribbons. *Phys. Rev. B* **2008**, *78*, 245402.
- (27) Tao, C.; Jiao, L.; Yazyev, O. V.; Chen, Y.-C.; Feng, J.; Zhang, X.; Capaz, R. B.; Tour, J. M.; Zettl, A.; Louie, S. G.; Dai, H.; Crommie, M. F. Spatially resolving edge states of chiral graphene nanoribbons. *Nature Physics* **2011**, *7*, 616–620.
- (28) Joost, J.-P.; Schlünzen, N.; Bonitz, M. Femtosecond Electron Dynamics in Graphene Nanoribbons – A Nonequilibrium Green Functions Approach Within an Extended Hubbard Model. *Phys. Status Solidi B* **2019**, *256*, 1800498.
- (29) Yazyev, O. V.; Capaz, R. B.; Louie, S. G. Theory of magnetic edge states in chiral graphene nanoribbons. *Phys. Rev. B* **2011**, *84*, 115406.
- (30) Tersoff, J.; Hamann, D. R. Theory of the scanning tunneling microscope. *Phys. Rev. B* **1985**, *31*, 805–813.
- (31) Meunier, V.; Lambin, P. Tight-Binding Computation of the STM Image of Carbon Nanotubes. *Phys. Rev. Lett.* **1998**, *81*, 5588–5591.
- (32) Magda, G. Z.; Jin, X.; Hagymási, I.; Vancsó, P.; Osváth, Z.; Nemes-Incze, P.; Hwang, C.; Biró, L. P.; Tapasztó, L. Room-temperature magnetic order on zigzag edges of narrow graphene nanoribbons. *Nature* **2014**, *514*, 608–611.
- (33) Pisani, L.; Chan, J. A.; Montanari, B.; Harrison, N. M. Electronic structure and magnetic properties of graphitic ribbons. *Phys. Rev. B* **2007**, *75*, 064418.
- (34) van der Lit, J.; Boneschanscher, M. P.; Vanmaekelbergh, D.; Ijäs, M.; Uppstu, A.; Ervasti, M.; Harju, A.; Liljeroth, P.; Swart, I. Suppression of electron-phonon coupling in graphene nanoribbons contacted via a single atom. *Nature Communications* **2013**, *4*, 2023.
- (35) Wang, S.; Talirz, L.; Pignedoli, C. A.; Feng, X.; Müllen, K.; Fasel, R.; Ruffieux, P. Giant edge state splitting at atomically precise graphene zigzag edges. *Nat. Commun.* **2016**, *7*, 11507.
- (36) Feldner, H.; Meng, Z. Y.; Lang, T. C.; Assaad, F. F.; Wessel, S.; Honecker, A. Dynamical Signatures of Edge-State Magnetism on Graphene Nanoribbons. *Phys. Rev. Lett.* **2011**, *106*, 226401.
- (37) Fernández-Rossier, J.; Palacios, J. J. Magnetism in Graphene Nanoislands. *Phys. Rev. Lett.* **2007**, *99*, 177204.
- (38) Feldner, H.; Meng, Z. Y.; Honecker, A.; Cabra, D.; Wessel, S.; Assaad, F. F. Magnetism of finite graphene samples: Mean-field theory compared with exact diagonalization and quantum Monte Carlo simulations. *Phys. Rev. B* **2010**, *81*, 115416.
- (39) Golor, M.; Koop, C.; Lang, T. C.; Wessel, S.; Schmidt, M. J. Magnetic Correlations in Short and Narrow Graphene Armchair Nanoribbons. *Phys. Rev. Lett.* **2013**, *111*, 085504.
- (40) Ortiz, R.; García-Martínez, N. A.; Lado, J. L.; Fernández-Rossier, J. Electrical spin manipulation in graphene nanostructures. *Phys. Rev. B* **2018**, *97*, 195425.
- (41) Lee, Y.-L.; Zhao, F.; Cao, T.; Ihm, J.; Louie, S. G. Topological Phases in Cove-Edged and Chevron Graphene Nanoribbons: Geometric Structures, Z₂ Invariants, and Junction States. *Nano Lett.* **2018**, *18*, 7247–7253.
- (42) Lin, K.-S.; Chou, M.-Y. Topological Properties of Gapped Graphene Nanoribbons with Spatial Symmetries. *Nano Lett.* **2018**, *18*, 7254–7260.

Graphical TOC Entry

